

Chemical Design Principles for Cache-Type Sc–Sb–Te Phase-Change Memory Materials

Getasew M. Zewdie,^{†,‡} Yuxing Zhou,^{†,‡} Liang Sun,[‡] Feng Rao,[§] Volker L. Deringer,^{||} Riccardo Mazzarello,[⊥] and Wei Zhang^{*,†}

[†]Center for Advancing Materials Performance from the Nanoscale, State Key Laboratory for Mechanical Behavior of Materials, Xi'an Jiaotong University, Xi'an 710049, China

[‡]Key Laboratory of Materials Processing Engineering, College of Materials Science and Engineering, Xi'an Shiyou University, Xi'an 710065, China

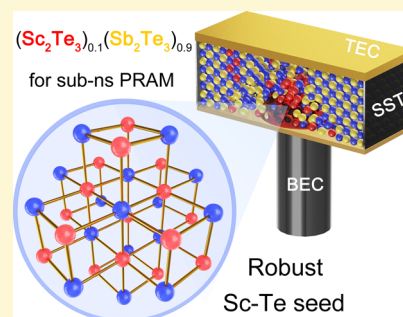
[§]College of Materials Science and Engineering, Shenzhen University, Shenzhen 518060, China

^{||}Department of Engineering, University of Cambridge, Cambridge CB2 1PZ, U.K.

[⊥]Institute for Theoretical Solid-State Physics, JARA-FIT and JARA-HPC, RWTH Aachen University, Aachen 52056, Germany

Supporting Information

ABSTRACT: Enhanced crystal nucleation in a Sc–Sb–Te phase-change material has enabled subnanosecond switching in phase-change memory devices, making cache-type nonvolatile memory feasible. However, the microscopic mechanisms remain to be further explored. In this work, we present a systematic ab initio study of the relevant parent compounds, namely, Sc_2Te_3 and Sb_2Te_3 . Despite similar bond lengths and angles in the amorphous phases of the two compounds, Sc_2Te_3 displays a much more ordered amorphous network without homopolar bonds. As a result, the local structural order in amorphous Sc_2Te_3 is dominated by square motifs, remarkably similar to those of the metastable rocksalt-like phase. Chemical bonding analysis indicates more robust Sc–Te bonds compared with Sb–Te bonds in the amorphous phase, as well as a substantial role of electrostatic interactions in Sc_2Te_3 but not in Sb_2Te_3 . The robustness of Sc–Te bonds explains the enhanced nucleation in Sc–Sb–Te compounds. Finally, we discuss an alloying strategy of Sc_2Te_3 and Sb_2Te_3 for cache-type Sc–Sb–Te-based phase-change memory.



INTRODUCTION

In the information era, the exponentially increasing demand for data storage and processing is posing a serious challenge for current silicon-based electronic devices.¹ New technologies and new materials are being pursued to cope with this problem.¹ Nonvolatile memory^{2–6} and neuro-inspired computing^{6–9} are two promising routes for substantial improvement of computing efficiency, as the former optimizes the memory hierarchy, and the latter unifies computing with storage in the same memory cell. Among the emerging materials for these two technologies,¹ chalcogenide phase-change materials (PCMs)^{2,6} stand out as the most mature candidate, owing to their robust working mechanism and their high compatibility with the complementary metal–oxide–semiconductor technology.¹⁰ Competitive phase-change memory products have been released recently, and are expected to lead to a major change in data-intensive applications.¹¹

Phase-change memory exploits the large electrical resistance contrast between the amorphous and crystalline state of PCMs, such as $\text{Ge}_2\text{Sb}_2\text{Te}_5$ (GST),^{12–16} to enable digital data storage.^{2,3} The switching between the two states is accomplished by rapid and reversible structural transitions at elevated temperatures, leading to switching times on the order

of tens of nanoseconds.^{17–20} Yet, the two states are thermally robust at room temperature for decades in the absence of power supply, ensuring long-term data storage. RESET operations (amorphization) can be accomplished within 1 nanosecond, whereas SET operations (crystallization) need much longer time. Preprogramming strategies were developed to speed up the SET process of GST devices to enter the subnanosecond regime.^{17,21} More recently, systematic screening across the periodic table led to the design of a new material, namely, $\text{Sc}_{0.2}\text{Sb}_{0.8}\text{Te}_3$ (“SST” in the following), which was shown to enable subnanosecond SET operations even in the absence of a pretreatment.²² This intrinsic material approach extends the capability of phase-change memory to compete with cache memory—static random access memory in terms of both switching speed and operation frequency. Taking into account the nonvolatile feature of SST, this new material opens up the possibility to build a universal memory²³ using phase-change devices.

Received: February 3, 2019

Revised: April 24, 2019

Published: April 25, 2019

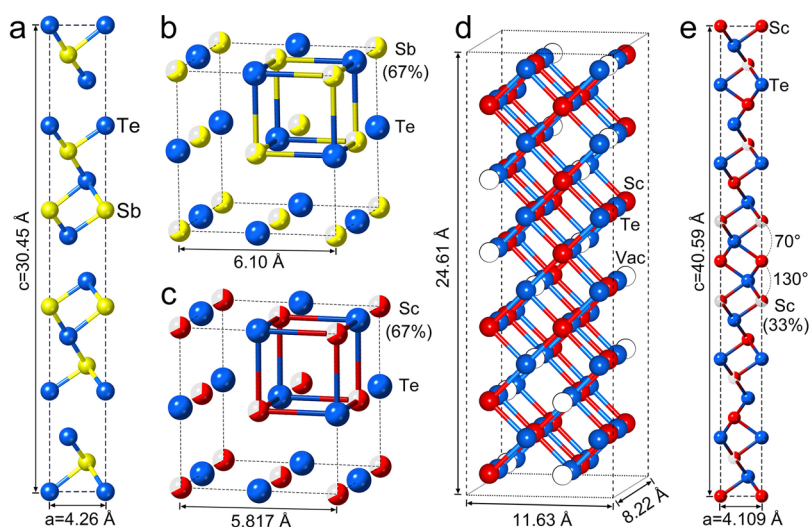


Figure 1. Crystal structures of Sc_2Te_3 and Sb_2Te_3 . (a) Rhombohedral Sb_2Te_3 (in the conventional hexagonal cell setup). The Sb–Te bond lengths are 2.97 and 3.13 Å. (b,c) Rocksalt-like Sb_2Te_3 and Sc_2Te_3 . The Sb–Te and Sc–Te bond lengths are ~ 3.05 and ~ 2.91 Å, respectively. 2/3 of the cation sites are occupied, as indicated by partially filled spheres. Four-membered rings as the defining structural motif are highlighted. (d) Orthorhombic Sc_2Te_3 . Atomic vacancies are arranged in an ordered fashion. The Sc–Te bond length is ~ 2.90 Å. (e) Rhombohedral Sc_2Te_3 . The occupancy for one of the Sc sites (6c) is 1/3, as indicated by partially filled spheres, whereas the others (3a and 3b) are fully occupied; see ref 37. The Sc–Te bond length is ~ 2.95 Å.

The technologically relevant properties of PCMs can be largely traced back to the atomic-scale structure and the dynamics of the microscopic constituents. The abundance of structural fragments that can serve as crystalline precursors—namely, ABAB squares ($A = \text{Ge}$ or Sb , $B = \text{Te}$) in amorphous GST—is one key parameter for fast incubation,^{24–29} whereas the dynamical stability of ABAB squares at elevated temperatures is another one.²² In supercooled liquid GST, ABAB squares have a short lifetime. By contrast, ABAB squares are much more robust in supercooled liquid SST, thus reducing the stochasticity of nucleation and leading to an ultrafast incubation process.²² However, there remain open questions regarding the chemical properties and crystallization dynamics in SST. First, different crystalline polymorphs are known for both Sc_2Te_3 and Sb_2Te_3 ; how do they affect the crystallization tendency of SST? Second, what are the structural properties of the amorphous phases, and what are the bonding mechanisms at play? Finally, why does the concentration of Sc in SST need to be kept at a relatively small percentage for high performance of phase-change devices?

In this work, we perform thorough structural and chemical bonding characterizations of both crystalline and amorphous (a-) Sc_2Te_3 and Sb_2Te_3 , the two parent compounds of SST, based on *ab initio* simulations. We aim at understanding the nature of bonding in a- Sc_2Te_3 and a- Sb_2Te_3 , and the way by which it leads to the enhanced nucleation in SST. These atomistic and chemical insights are expected to drive further development of cache-type phase-change memory.

RESULTS AND DISCUSSION

Crystalline Parent Compounds. Polymorphism occurs for both crystalline Sb_2Te_3 and Sc_2Te_3 . The stable phase of Sb_2Te_3 is rhombohedral ($R\bar{3}m$) with alternately stacked Sb and Te layers forming quintuple blocks along the c axis.³⁰ Each unit cell contains three quintuple blocks and three gap layers (Figure 1a). In addition, a metastable defective rocksalt-like polymorph of Sb_2Te_3 was identified recently.³¹ This crystalline phase shares similar structural features as rocksalt-like

GST^{32–34} in that one sublattice is fully occupied by Te atoms, whereas the other one is randomly occupied by 2/3 Sb atoms and 1/3 vacancies (Figure 1b). Despite the high concentration of atomic vacancies, Peierls-like distortion around Sb atoms is found in this disordered rocksalt-like structure (Figure S1). In both polymorphs, Sb and Te atoms form heteropolar Sb–Te bonds exclusively, with bond angles close to 90° . As regards Sc_2Te_3 , three crystalline phases have been described. Similar to rocksalt-like Sb_2Te_3 , a defective rocksalt-like phase of Sc_2Te_3 exists (Figure 1c), which has a smaller lattice parameter³⁵ ($a \approx 5.817$ Å) than the one of Sb_2Te_3 ($a \approx 6.10$ Å).³¹ Another crystalline phase of Sc_2Te_3 forms an orthorhombic Sc_2S_3 -type structure with octahedral coordination.³⁶ The only difference between this phase and the rocksalt-like phase is that the 1/3 atomic vacancies on the cation sublattice are arranged in an ordered fashion (Figure 1d). The third crystalline phase of Sc_2Te_3 is a layered rhombohedral phase in space group $R\bar{3}m$ with alternating layers resembling cation-deficient B1-like (NaCl-type) and B8-like (NiAs-type) motifs stacked along the c axis; no gap layers are present here³⁷ (Figure 1e). Some cation layers consist of 1/3 Sc atoms and 2/3 atomic vacancies. All Sc atoms are octahedrally coordinated by Te. By contrast, some Te atoms form Sc–Te bonds with 70° and 130° bond angle near the B8-like fragments, in addition to the majority of octahedral Sc–Te bonds.

Density functional theory (DFT) calculations are performed by using the Perdew–Burke–Ernzerhof (PBE) functional (see more details in the Methods section). They show that rocksalt-like Sb_2Te_3 is ~ 75 meV/atom higher in total energy than the stable rhombohedral phase. The calculated cohesive energies are -0.06 and -0.12 eV/atom for rocksalt-like and rhombohedral Sb_2Te_3 , respectively. As regards Sc_2Te_3 , all three crystalline phases have a substantially more favorable cohesive energy than Sb_2Te_3 , that is -1.23 , -1.22 , and -1.15 eV/atom for orthorhombic, rhombohedral, and rocksalt-like Sc_2Te_3 , respectively. More precisely, our calculations reveal that the rocksalt-like phase and rhombohedral phase that

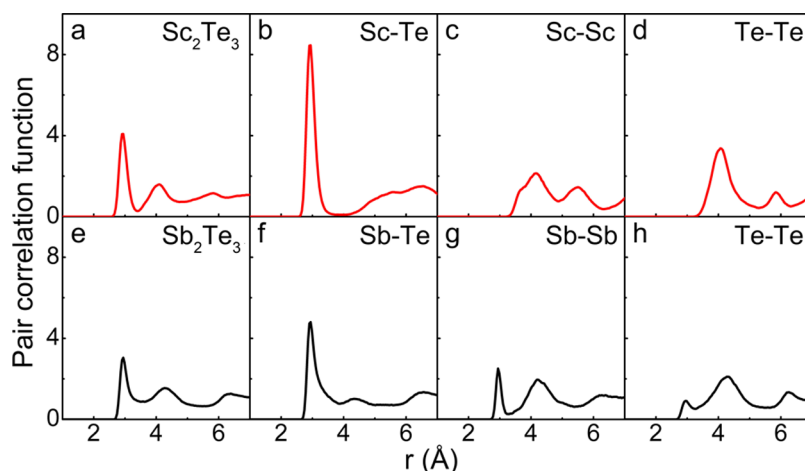


Figure 2. Atomic contacts in the amorphous phases, determined from the PCF. Data were collected based on a 10 ps AIMD trajectory at 300 K. (a–d) Total and partial PCFs of a-Sc₂Te₃. The positions of the first peak are 2.93 Å (total), 2.93 Å (Sc–Te), 4.14 Å (Sc–Sc), and 4.06 Å (Te–Te), respectively. (e–h) Total and partial PCFs of a-Sb₂Te₃. The position of the first peak is at ~2.93 Å for the total and the three partial PCFs.

contain strong disorder (i.e., randomly distributed atomic vacancies on the cation sublattice) are ~84 and ~13 meV/atom higher in total energy than the ordered orthorhombic phase (see [Methods](#)).

For Sb₂Te₃ and SST, a rocksalt-like structure is obtained upon rapid crystallization.²² However, the rhombohedral phase of Sc₂Te₃ deviates from the rocksalt-like phase with non-octahedral structural features, which could be present in the amorphous state of Sc-rich Sc–Sb–Te compounds as well. In terms of subnanosecond nucleation processes at evaluated temperatures, the nonoctahedral motifs might hinder the formation of nuclei, thus slowing down the SET operations of phase-change devices. Structural and bonding analyses of the amorphous phase discussed below provide further support that the concentration of Sc in Sc–Sb–Te compounds needs to be low.

Structure of the Amorphous Phases. An amorphous (a-) Sc₂Te₃ structural model was generated in melt-quench simulations ([Figure S2](#)). A 3 × 3 × 3 expansion of the rocksalt-like unit cell with the experimental lattice parameter was used as the starting configuration (180 atoms in a 17.58 × 17.58 × 17.58 Å³ box). It was quickly heated above 2000 K for randomization, and then quenched down to the melting temperature of ~1250 K and equilibrated there for 30 ps. Next, the liquid model was quenched down to 300 K within 50 ps and equilibrated at 300 K for 30 ps ([Figure S2](#)). The box size of the model was adjusted seven times during the quenching simulation to reduce the internal stress. A theoretical density of 0.0313 atom Å⁻³ was obtained for a-Sc₂Te₃, corresponding to a supercell of 17.91 × 17.91 × 17.91 Å³. Two additional a-Sc₂Te₃ models and three a-Sb₂Te₃ models (containing 180 atoms each) were generated with the same scheme. The theoretical density of 0.0271 atom Å⁻³ was used for a-Sb₂Te₃.³⁸ The structural features of a-Sb₂Te₃ discussed below are in good agreement with previous work.^{38–40} All three a-Sc₂Te₃ models give very similar results, and the same holds for a-Sb₂Te₃.

The (partial) pair correlation functions (PCFs) were calculated based on the ab initio molecular dynamics (AIMD) trajectories at 300 K ([Figure 2](#)). As regards the total PCF, a-Sc₂Te₃ ([Figure 2a](#)) shows a similar profile as compared with a-Sb₂Te₃ ([Figure 2e](#)), with similar peak

positions for both the first (~2.9 Å) and second peaks (~4.2 Å). This structural similarity guarantees the overall geometrical compatibility between the two amorphous materials. However, clear differences are observed at ~3.4 Å, in that the first valley of the total PCF is deeper in a-Sc₂Te₃ than in a-Sb₂Te₃, indicating much fewer chemical bonds in this length range in the Sc compound. Indeed, there is almost no contact between Sc and Te atoms between 3.3 and 4.2 Å, whereas a finite fraction of Sb–Te bonds is observed consistently in the same length range. Furthermore, a primary peak for homopolar Sb–Sb and Te–Te bonds is found at ~3.0 Å in a-Sb₂Te₃, but is absent in a-Sc₂Te₃, indicating a more ordered amorphous network in Sc₂Te₃. Based on the PCF data, we set a uniform cutoff at 3.3 Å for a-Sc₂Te₃, and separate cutoffs for a-Sb₂Te₃ with Sb–Te 3.4 Å, for Sb–Sb 3.3 Å, and Te–Te 3.2 Å, for further structural analyses. The choice of cutoffs for a-Sb₂Te₃ is in line with previous work.^{38,39}

[Figure 3a](#) shows the distribution of coordination numbers (CNs) in our systems. In a-Sc₂Te₃, the majority of Sc and Te

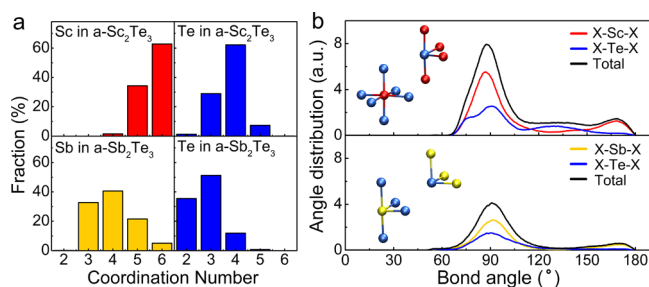


Figure 3. The local structural analysis for a-Sc₂Te₃ and a-Sb₂Te₃ at 300 K. (a) Distribution of CN and (b) ADF of a-Sc₂Te₃ and a-Sb₂Te₃. Insets in (b) show typical atomic configurations for Sc (CN = 6) and Te (CN = 4) atoms in a-Sc₂Te₃, and Sb (CN = 4) and Te (CN = 3) atoms in a-Sb₂Te₃.

atoms are six- and four-fold coordinated, whereas in a-Sb₂Te₃, most Sb and Te atoms are four- and three-fold coordinated. Note that, in the rocksalt-like phases, Sc and Sb have six-fold coordination, whereas Te atoms are, on average, four-fold coordinated due to the presence of vacancies. The angular distribution functions (ADF) show a prominent feature of octahedral configuration with a major peak around 90° and a

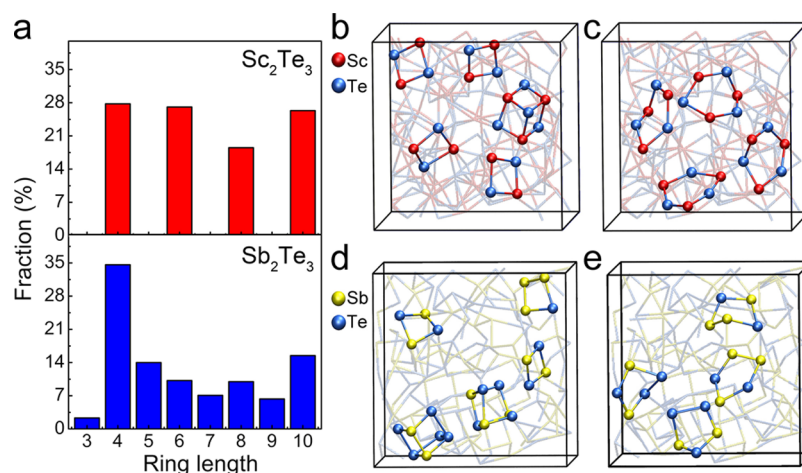


Figure 4. Medium range order in a- Sc_2Te_3 and a- Sb_2Te_3 at 300 K. (a) Statistics for primitive rings: note the absence of any odd-membered rings in the Sc phase. (b–e) Snapshots of typical four- and six-membered primitive rings in a- Sc_2Te_3 (the former resembling the crystalline phase; cf. Figure 1b,c), and typical four- and five-membered primitive rings in a- Sb_2Te_3 . In both amorphous phases, the bonding angles in four-membered rings are close to 90° , whereas higher-membered rings typically include nonoctahedral-like structural fragments.

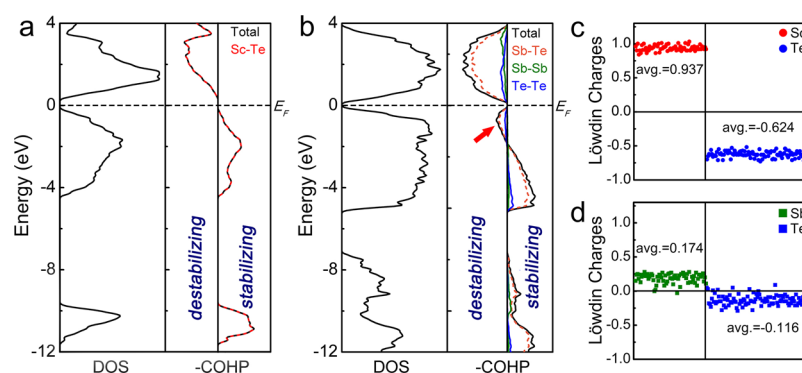


Figure 5. Chemical bonding in a- Sc_2Te_3 and a- Sb_2Te_3 . (a,b) DOS and COHP analysis for a- Sc_2Te_3 and a- Sb_2Te_3 . Contributions from all atomic contacts up to 3.4 Å were collected for COHP analyses. (c,d) Löwdin charges (in electrons per atom) of a- Sc_2Te_3 and a- Sb_2Te_3 . The x-axis is an arbitrary running index, and average values are given for all atomic species.

small peak near 170° in both compounds (Figure 3b). A major difference between the two structures is that a shoulder and a small peak appear around 70° and 130° for Te atoms in a- Sc_2Te_3 , corresponding to the nonoctahedral bonding environments that are observed in the rhombohedral phase of Sc_2Te_3 . Typical structural motifs of the two phases are shown in Figure 3b. The preponderance of (defective-) octahedral coordination is confirmed by computing the local order parameter,³⁸

$$q = 1 - \frac{3}{8} \sum_{i>k} \left(\frac{1}{3} + \cos \theta_{ijk} \right)^2$$

where the sum runs over pairs of atoms (i and k) bonded to a central atom (j). No tetrahedral motifs ($q > 0.8$) are identified in a- Sb_2Te_3 . With regard to a- Sc_2Te_3 , all Sc atoms are octahedrally coordinated, whereas a small fraction of Te atoms ($\sim 5\%$) is found in tetrahedral coordination. Overall, the dominant octahedral motifs closely resemble the local structure in the defective rocksalt-like crystals (Figure 1c,d).^{22,31}

The analysis of primitive (“shortest-path”) rings is typically used to understand the medium-range order of amorphous networks. An ideal rocksalt lattice consists of four-membered rings (ABAB squares). In the amorphous phase, more complex rings can emerge. The distribution of primitive rings up to ten-fold for the two compounds is shown in Figure 4a. Four-

membered rings are the dominant structural fragment in a- Sb_2Te_3 , whereas other even- and odd-membered rings are also observed. By contrast, comparable fractions of four-, six-, eight-, and ten-membered primitive rings are found in a- Sc_2Te_3 , whereas odd-membered rings are completely absent (Figure 4a). ABAB squares with A = Sc or Sb and B = Te represent the smallest crystal units in recrystallized SST. In a- Sb_2Te_3 , ABAB squares constitute $\sim 80\%$ of the four-membered primitive rings, whereas rest of them are in AAAB or ABAB forms. But in a- Sc_2Te_3 , all four-membered primitive rings are ABAB squares. These structural differences between the two compounds stem from the absence of homopolar bonds in Sc_2Te_3 , as to form odd-membered primitive rings, at least one pair of homopolar bonds must be present. Typical ring motifs found in our simulations of a- Sc_2Te_3 and a- Sb_2Te_3 are shown in Figure 4b–e. This property explains why, upon alloying Sc atoms into Sb_2Te_3 , the number of high-quality crystalline precursors consisting of ABAB squares increases.

Electronic and Bonding Nature. Next, we carry out the chemical bonding analyses of the two amorphous compounds using the crystal orbital Hamilton population (COHP) method.^{41–43} This method dissects the electronic density of states (DOS) into bonding (stabilizing) interaction and antibonding (destabilizing) interaction, revealing the chemical stability of compounds. Both a- Sc_2Te_3 and a- Sb_2Te_3 models

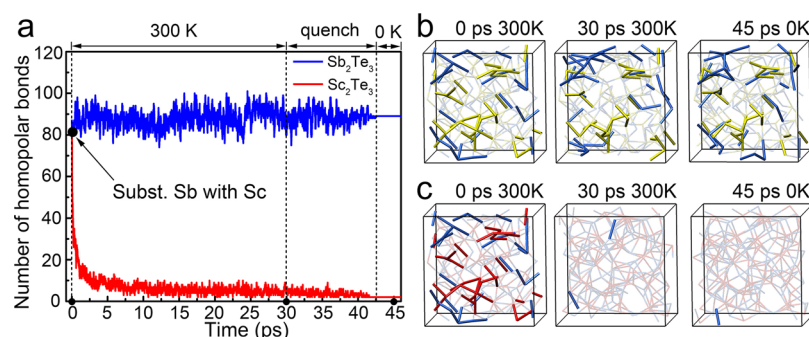


Figure 6. Strong relaxation of a- Sc_2Te_3 in the presence of homopolar bonds. (a) Statistics of homopolar bonds for melt-quenched a- Sb_2Te_3 (blue) and a hypothetical a- Sc_2Te_3 structure created by chemical substitution (red). The starting configuration is obtained by substituting all Sb atoms with Sc atoms in the a- Sb_2Te_3 model and re-scaling the cell volume to match that of our melt-quenched a- Sc_2Te_3 models. (b,c) Evolution of homopolar bonds (drawn as thick colored sticks) in the simulations. Yellow, red, and blue bonds represent Sb–Sb, Sc–Sc, and Te–Te bonds, respectively.

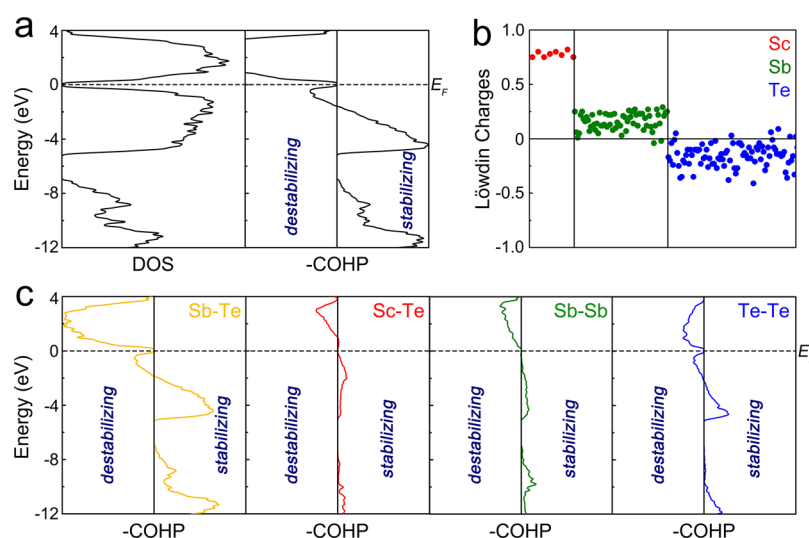


Figure 7. Chemical bonding analysis of a-SST. The model contains 8 Sc, 64 Sb, and 108 Te atoms in a $18.75 \times 18.75 \times 18.75 \text{ \AA}^3$ supercell, corresponding to the theoretical density of the amorphous phase. Both the atomic positions and volume are relaxed at 0 K. (a,b) DOS, COHP, and Löwdin charge analyses for a-SST. (c) COHP plots resolved according to Sb–Te, Sc–Te, Sb–Sb, and Te–Te bonds, collected over all occurrences of the respective contact in the simulation cell. Sc–Sc and Sc–Sb bonds are not found in the amorphous models. Contributions from all atomic contacts up to 3.4 Å were collected for COHP analyses.

were quenched down and optimized at 0 K for the DOS and COHP calculations. DFT calculations (using the PBE functional) show that rhombohedral Sb_2Te_3 has a narrow band gap of 0.15 eV,⁴⁴ whereas no band gap is found for all three crystalline phases of Sc_2Te_3 (Figure S3). With regard to the amorphous phase, finite band gaps are found for both a- Sc_2Te_3 (~ 0.25 eV) and a- Sb_2Te_3 (~ 0.1 eV), see Figure S4b. This suggests a metal-to-semiconductor transition for Sc_2Te_3 upon amorphization. The closed band gap in rhombohedral Sc_2Te_3 is due to defect states brought by the high amount of atomic vacancies, as a finite gap of ~ 0.2 eV can be obtained if Sc_2Te_3 takes the crystal structure of rhombohedral Sb_2Te_3 , where no vacancies are present (Figure S4). As regards the bonding, both amorphous structures are free from antibonding interaction directly at the Fermi level, indicating good chemical stability of the two phases (Figure S4a,b). For a- Sc_2Te_3 , all filled bands up to the E_F contribute to stabilization of the system, whereas there exists a finite antibonding interaction region below E_F in a- Sb_2Te_3 , indicating a potential source of instability of the system. To make a more direct comparison, we create a hypothetical a- Sb_2Te_3 model to rule out the effects

of homopolar bonds: for this, we take an a- Sc_2Te_3 structure and substitute all Sc atoms with Sb atoms in exactly the same geometrical configuration, including the atomic position and the lattice parameter, and perform the COHP analysis for the resulting model. In this configuration, all bond contributions are made by Sb–Te bonds, and the antibonding interaction below the E_F is still present (Figure S5). Overall, we can conclude that a- Sc_2Te_3 is chemically more robust than a- Sb_2Te_3 . These bonding features are in line with those found in the crystalline structures²² (Figure S5).

The absence of homopolar bonds leads to better defined crystalline precursors—ABAB squares and cubes in a- Sc_2Te_3 (Figure 4b). To further understand these structural features, we create a hypothetical a- Sc_2Te_3 model in which all Sb atoms in an a- Sb_2Te_3 configuration are substituted with Sc atoms, forming a finite fraction of homopolar Sc–Sc and Te–Te bonds (Figure 6). The presence of these homopolar bonds leads to a high penalty in total energy of ~ 600 meV/atom, which drives a strong relaxation of the system even at room temperature (Figure 6c). All of the homopolar bonds vanish quickly at room temperature, forming perfect ABAB squares

and cubes again. This tendency can be qualitatively understood based on the difference in electronegativity of the constituent elements: this difference is much larger for the pair Sc/Te than for Sb/Te, leading to a stronger charge transfer in a- Sc_2Te_3 . More quantitative information about individual atomic charges can be obtained from first-principles calculations: for this purpose, we use the same local-basis projection scheme as for the COHP analysis and now compute Löwdin charges⁴⁵ (Figure 5c). Clearly, in a- Sc_2Te_3 , atoms are more ionic than in a- Sb_2Te_3 , which increases the Coulomb repulsion between atoms with the same type of charge, resulting in a stronger energy penalty. Such ionic character is also present in the crystalline phases of Sc_2Te_3 (Figure S3).

Implications for Memory Devices. In typical phase-change memory devices based on GST or SST, the thickness of PCM layers amounts to several tens to a few hundred nanometers, and nucleation plays a leading role for crystallization.⁶ Although not determined precisely, the size of critical nuclei in SST is estimated to be several tens of atoms at ~ 600 K, corresponding to several connected cubes.²² The commercialized GST-based phase-change random access memory (PRAMs) suffer from the stochastic incubation process for nucleation in that the abundant crystalline precursors (ABAB squares and cubes) break and reform rapidly with a very short lifetime of ~ 5 ps at elevated temperatures, for example ~ 600 K. By contrast, Sc–Te bonds are typically more robust and can stay intact over long periods of time at 600 K. Here, our direct chemical bonding analyses of amorphous SST provide additional theoretical support for this scenario (Figure 7). The overall DOS and COHP curves of a-SST look similar to those of a- Sb_2Te_3 in that an antibonding region is found right below the Fermi level (Figure 7a). Resolving the COHP contributions to individual types of neighboring species reveals that this antibonding interaction is mainly contributed by Sb–Te and Te–Te bonds (Figure 7c). However, a stabilizing bonding interaction is observed for Sc–Te bonds in this energy range (Figure 7c). Moreover, the Löwdin charge analysis shows a more ionic character of Sc atoms in a-SST (Figure 7b), which results in the absence of homopolar Sc–Sc bonds because of the high energy penalty for cation–cation repulsion. The bonding nature of Sc atoms in a-SST generates high-quality and high-strength Sc–Te squares and cubes, thereby suppressing the stochasticity of incubation for ultrafast SET operations in SST-based PRAMs.

Our simulations reveal that Sc-centered local motifs in amorphous and all three crystalline states of Sc_2Te_3 always exhibit perfect or defective octahedral configuration, whereas a fraction of Te atoms in both rhombohedral and amorphous states tends to form nonoctahedral bonds, which also result in higher-membered rings in the amorphous structure, deviating from the rocksalt one (Figure 4c). Given the robustness of Sc–Te bonds, the nonoctahedral bonds and six-membered primitive rings may stay intact over long period of time at ~ 600 K, hindering crystallization into rocksalt-like structure. Our findings thus indicate that too much addition of Sc should be avoided for high-speed Sc–Sb–Te phase-change memory devices. Given a limited concentration of Sc, such as 4% atomic percent in SST (10% Sc_2Te_3 and 90% Sb_2Te_3), Te atoms would have a very low probability of forming nonoctahedral Sc–Te–Sc bonds in the Sc-poor environment. Another effect brought by the overconcentration of Sc is an increased viscosity²² stemming from the strong, partly-ionic Sc–Te chemical bonds. On the one hand, the latter effect

stabilizes the amorphous phase at low temperature for longer data retention, but, on the other hand, it reduces the atomic mobility at elevated temperatures, slowing down the crystal growth of SST and impeding the subnanosecond SET operations. The so-derived chemical design principles for high-performance cache-type Sc–Sb–Te PCM are summarized in Figure 8.

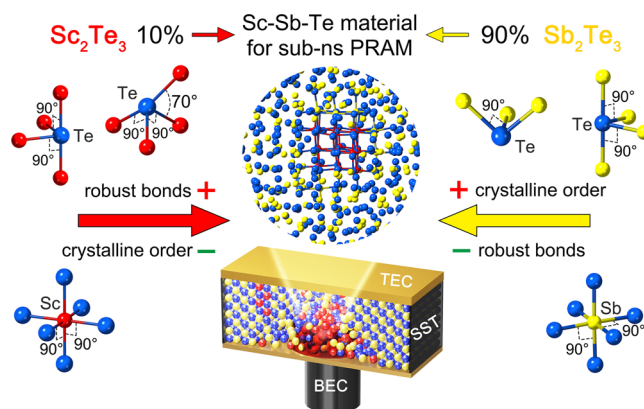


Figure 8. The chemical design principles for cache-type Sc–Sb–Te compounds. When a limited fraction of Sc_2Te_3 (10%) is alloyed into Sb_2Te_3 (90%), the SST compound (4% Sc) can take advantages of both parent compounds to undergo ultrafast nucleation with high-quality and robust Sc–Te crystalline precursors and subsequent rapid crystal growth of Sb–Te components. Thus, subnanosecond SET operations can be achieved in conventional PRAM cells with SST PCM. The top and bottom electrode contact are abbreviated as TEC and BEC.

CONCLUSIONS

In summary, the structural and chemical bonding properties of amorphous Sc_2Te_3 and Sb_2Te_3 have been clarified by comprehensive ab initio simulations. Our structural analyses reveal good geometrical compatibility between the two amorphous phases, whereas a- Sc_2Te_3 has a better defined local geometry. The absence of homopolar bonds in a- Sc_2Te_3 is attributed to strong charge transfer, and to the resulting high energy penalty for homopolar bonds. Although a- Sc_2Te_3 exhibits high chemical stability, our simulations also indicate that too large Sc concentrations in the Sc–Sb–Te alloy need to be avoided, as the increased medium-range order brought by a- Sc_2Te_3 would drive the amorphous structure away from the local order in the targeted crystalline counterparts, increasing structural complexity that impedes rapid nucleation. In contrast, alloying a small amount of Sc_2Te_3 into Sb_2Te_3 , better-defined and chemically more robust ABAB squares and cubes enable enhanced nucleation in the resulting SST material, thereby enabling subnanosecond memory operations.

METHODS

The structural relaxation and self-consistent electronic-structure calculations based on DFT were carried out using the Vienna Ab initio simulation package, with a plane wave cutoff of 500 eV, the projector augmented-wave pseudopotentials,⁴⁶ and the PBE functional.⁴⁷ All crystalline models are calculated by using the experimental lattice parameters. For rhombohedral and rocksalt Sc_2Te_3 and rocksalt Sb_2Te_3 , three independent models, where the positions of atomic vacancies are generated by a random number generator, are calculated for each crystalline phase. The averaged energy values are taken for the calculation of energy difference. More

details about the crystalline Sc_2Te_3 can be found in Figure S3. The chemical bonding analysis was performed using the COHP method,^{41–43} as implemented in the local orbital basis suite towards electronic-structure reconstruction (LOBSTER).⁴⁸ This bonding analysis tool reads the wave functions from plane-wave DFT calculations,⁴⁹ and projects them onto localized orbitals, thereby making large and complex structural models readily accessible to a chemical interpretation. In the recent years, this approach has been applied to highly disordered crystalline^{22,50,51} and even amorphous PCMs.^{52–54} More recently, charge analyses have been implemented in LOBSTER, making it possible to assign Löwdin atomic charges based on the same projection scheme and thereby analyzing both the covalent and the electrostatic nature of the system.⁵⁵ DFT based AIMD simulations were carried out using the second-generation Car–Parrinello scheme,⁵⁶ implemented in the Quickstep code of the CP2K package.⁵⁷ The code uses a mixed scheme of Gaussian-type basis sets and plane waves. The Kohn–Sham orbitals were expanded in basis sets with triple-zeta plus polarization quality. Plane waves with a cutoff of 300 Ry were used to expand the charge density. The Goedecker pseudopotentials⁵⁸ and the PBE functional⁵⁷ were used. The Brillouin zone was sampled at the Γ point of the supercell. AIMD simulations were performed in the canonical ensemble (NVT) with a stochastic Langevin thermostat. The time step was 2 fs. During quenching simulations, the size of the supercell was adjusted seven times, and each simulation was an independent NVT run.

■ ASSOCIATED CONTENT

● Supporting Information

The Supporting Information is available free of charge on the ACS Publications website at DOI: 10.1021/acs.chemmater.9b00510.

Pierls-like distortion analysis, schematic descriptions of melt-quench simulations, and chemical bonding and charge analyses for various phases of Sc_2Te_3 and Sb_2Te_3 (PDF)

■ AUTHOR INFORMATION

Corresponding Author

*E-mail: wzhang0@mail.xjtu.edu.cn.

ORCID

Yuxing Zhou: 0000-0001-8061-3867

Volker L. Deringer: 0000-0001-6873-0278

Wei Zhang: 0000-0002-0720-4781

Author Contributions

*G.M.Z. and Y.Z. contributed equally.

Notes

The authors declare no competing financial interest.

■ ACKNOWLEDGMENTS

W.Z. thanks the support of National Natural Science Foundation of China (61774123), 111 Project 2.0 (BP2018008), the Science and Technology Department of Jiangsu Province (BK20170414), and the Young Talent Support Plan of Xi'an Jiaotong University. G.M.Z. acknowledges scholarship support from Chinese Scholarship Council. V.L.D. acknowledges a Leverhulme Early Career Fellowship and support from the Isaac Newton Trust. R.M. acknowledges funding from Deutsche Forschungsgemeinschaft within SFB 917 “Nanoswitches”. F.R. gratefully thanks the National Natural Science Foundation of China (61622408), the Major Provincial Basic Research Program of Guangdong (2017KZDXM070), and the Science and Technology Foundation of Shenzhen (JCYJ20180507182248605, JCYJ20170302150053136). The authors also acknowledge

the support by the HPC platform of Xi'an Jiaotong University and the International Joint Laboratory for Micro/Nano Manufacturing and Measurement Technologies of Xi'an Jiaotong University.

■ REFERENCES

- (1) Wong, H.-S. P.; Salahuddin, S. Memory leads the way to better computing. *Nat. Nanotechnol.* **2015**, *10*, 191–194.
- (2) Wuttig, M.; Yamada, N. Phase-change materials for rewritable data storage. *Nat. Mater.* **2007**, *6*, 824–832.
- (3) Wong, H.-S. P.; Raoux, S.; Kim, S.; Liang, J.; Reifenberg, J. P.; Rajendran, B.; Asheghi, M.; Goodson, K. E. Phase Change Memory. *Proc. IEEE* **2010**, *98*, 2201.
- (4) Zhang, W.; Ma, E. Single-element glass to record data. *Nat. Mater.* **2018**, *17*, 654–655.
- (5) Salinga, M.; Kersting, B.; Ronneberger, I.; Jonnalagadda, V. P.; Vu, X. T.; Le Gallo, M.; Giannopoulos, I.; Cojocaru-Mirédin, O.; Mazzarello, R.; Sebastian, A. Monatomic phase change memory. *Nat. Mater.* **2018**, *17*, 681–685.
- (6) Zhang, W.; Mazzarello, R.; Wuttig, M.; Ma, E. Designing crystallization in phase-change materials for universal memory and neuro-inspired computing. *Nat. Rev. Mater.* **2019**, *4*, 150–168.
- (7) Kuzum, D.; Jeyasingh, R. G. D.; Lee, B.; Wong, H.-S. P. Nanoelectronic programmable synapses based on phase change materials for brain-inspired computing. *Nano Lett.* **2012**, *12*, 2179–2186.
- (8) Ambrogio, S.; Narayanan, P.; Tsai, H.; Shelby, R. M.; Boybat, I.; di Nolfo, C.; Sidler, S.; Giordano, M.; Bodini, M.; Farinha, N. C. P.; Killeen, B.; Cheng, C.; Jaoudi, Y.; Burr, G. W. Equivalent-accuracy accelerated neural-network training using analogue memory. *Nature* **2018**, *558*, 60–67.
- (9) Tuma, T.; Pantazi, A.; Le Gallo, M.; Sebastian, A.; Eleftheriou, E. Stochastic phase-change neurons. *Nat. Nanotechnol.* **2016**, *11*, 693–699.
- (10) Fong, S. W.; Neumann, C. M.; Wong, H.-S. P. Phase-Change Memory-Towards a Storage-Class Memory. *IEEE Trans. Electron Devices* **2017**, *64*, 4374–4385.
- (11) Hruska, J. Intel Announces New Optane DC Persistent Memory. <https://www.extremetech.com/extreme/270270-intel-announces-new-optane-dc-persistent-memory> (accessed May 31, 2018).
- (12) Yamada, N.; Ohno, E.; Nishiuchi, K.; Akahira, N.; Takao, M. Rapid-phase transitions of $\text{GeTe-Sb}_2\text{Te}_3$ pseudobinary amorphous thin films for an optical disk memory. *J. Appl. Phys.* **1991**, *69*, 2849–2856.
- (13) Kolobov, A. V.; Fons, P.; Frenkel, A. I.; Ankudinov, A. L.; Tominaga, J.; Uruga, T. Understanding the phase-change mechanism of rewritable optical media. *Nat. Mater.* **2004**, *3*, 703–708.
- (14) Sun, Z.; Zhou, J.; Ahuja, R. Structure of Phase Change Materials for Data Storage. *Phys. Rev. Lett.* **2006**, *96*, 055507.
- (15) Kooi, B. J.; Groot, W. M. G.; De Hosson, J. T. M. In situ transmission electron microscopy study of the crystallization of $\text{Ge}_2\text{Sb}_2\text{Te}_5$. *J. Appl. Phys.* **2004**, *95*, 924.
- (16) Wang, J.-J.; Wang, J.; Du, H.; Lu, L.; Schmitz, P. C.; Reindl, J.; Mio, A. M.; Jia, C.-L.; Ma, E.; Mazzarello, R.; Wuttig, M.; Zhang, W. Genesis and Effects of Swapping Bilayers in Hexagonal GeSb_2Te_4 . *Chem. Mater.* **2018**, *30*, 4770–4777.
- (17) Loke, D.; Lee, T. H.; Wang, W. J.; Shi, L. P.; Zhao, R.; Yeo, Y. C.; Chong, T. C.; Elliott, S. R. Breaking the speed limits of phase-change memory. *Science* **2012**, *336*, 1566–1569.
- (18) Orava, J.; Greer, A. L.; Gholipour, B.; Hewak, D. W.; Smith, C. E. Characterization of supercooled liquid $\text{Ge}_2\text{Sb}_2\text{Te}_5$ and its crystallization by ultrafast-heating calorimetry. *Nat. Mater.* **2012**, *11*, 279–283.
- (19) Zalden, P.; von Hoegen, A.; Landreman, P.; Wuttig, M.; Lindenberg, A. M. How Supercooled Liquid Phase-Change Materials Crystallize: Snapshots after Femtosecond Optical Excitation. *Chem. Mater.* **2015**, *27*, 5641–5646.

- (20) Behrens, M.; Lotnyk, A.; Gerlach, J. W.; Hilmi, I.; Abel, T.; Lorenz, P.; Rauschenbach, B. Ultrafast interfacial transformation from 2D- to 3D-bonded structures in layered Ge-Sb-Te thin films and heterostructures. *Nanoscale* **2018**, *10*, 22946–22953.
- (21) Loke, D. K.; Skelton, J. M.; Lee, T. H.; Zhao, R.; Chong, T.-C.; Elliott, S. R. Ultrafast Nanoscale Phase-Change Memory Enabled By Single-Pulse Conditioning. *ACS Appl. Mater. Interfaces* **2018**, *10*, 41855–41860.
- (22) Rao, F.; Ding, K.; Zhou, Y.; Zheng, Y.; Xia, M.; Lv, S.; Song, Z.; Feng, S.; Ronneberger, I.; Mazzarello, R.; Zhang, W.; Ma, E. Reducing the stochasticity of crystal nucleation to enable subnanosecond memory writing. *Science* **2017**, *358*, 1423–1427.
- (23) Wuttig, M. Towards a universal memory? *Nat. Mater.* **2005**, *4*, 265–266.
- (24) Kohara, S.; Kato, K.; Kimura, S.; Tanaka, H.; Usuki, T.; Suzuya, K.; Tanaka, H.; Moritomo, Y.; Matsunaga, T.; Yamada, N.; Tanaka, Y.; Suematsu, H.; Takata, M. Structural basis for the fast phase change of Ge₂Sb₂Te₅: Ring statistics analogy between the crystal and amorphous states. *Appl. Phys. Lett.* **2006**, *89*, 201910.
- (25) Akola, J.; Jones, R. Structural phase transitions on the nanoscale: The crucial pattern in the phase-change materials Ge₂Sb₂Te₅ and GeTe. *Phys. Rev. B: Condens. Matter Mater. Phys.* **2007**, *76*, 235201.
- (26) Hegedüs, J.; Elliott, S. R. Microscopic origin of the fast crystallization ability of Ge-Sb-Te phase-change memory materials. *Nat. Mater.* **2008**, *7*, 399–405.
- (27) Ronneberger, I.; Zhang, W.; Eshet, H.; Mazzarello, R. Crystallization properties of the Ge₂Sb₂Te₅ phase-change compound from advanced simulations. *Adv. Funct. Mater.* **2015**, *25*, 6407–6413.
- (28) Ronneberger, I.; Zhang, W.; Mazzarello, R. Crystal growth of Ge₂Sb₂Te₅ at high temperatures. *MRS Commun.* **2018**, *8*, 1018–1023.
- (29) Xu, M.; Cheng, Y.; Sheng, H.; Ma, E. Nature of Atomic Bonding and Atomic Structure in the Phase-Change Ge₂Sb₂Te₅ Glass. *Phys. Rev. Lett.* **2009**, *103*, 195502.
- (30) Belotskii, D. P.; Babyuk, P. F. The In₂Te₃-Sb₂Te₃ system. *Inorg. Chem.* **1970**, *6*, 505–507.
- (31) Zheng, Y.; Xia, M.; Cheng, Y.; Rao, F.; Ding, K.; Liu, W.; Jia, Y.; Song, Z.; Feng, S. Direct observation of metastable face-centered cubic Sb₂Te₃ crystal. *Nano Res.* **2016**, *9*, 3453–3462.
- (32) Yamada, N.; Matsunaga, T. Structure of laser-crystallized Ge₂Sb₂xTe₅ sputtered thin films for use in optical memory. *J. Appl. Phys.* **2000**, *88*, 7020–7028.
- (33) Zhang, B.; Zhang, W.; Shen, Z.; Chen, Y.; Li, J.; Zhang, S.; Zhang, Z.; Wuttig, M.; Mazzarello, R.; Ma, E.; Han, X. Element-resolved atomic structure imaging of rocksalt Ge₂Sb₂Te₅ phase-change material. *Appl. Phys. Lett.* **2016**, *108*, 191902.
- (34) Lotnyk, A.; Bernütz, S.; Sun, X.; Ross, U.; Ehrhardt, M.; Rauschenbach, B. Real-space imaging of atomic arrangement and vacancy layers ordering in laser crystallised Ge₂Sb₂Te₅ phase change thin films. *Acta Mater.* **2016**, *105*, 1–8.
- (35) Men'kov, A. A.; Komissarova, L. N.; Simanov, Y. P.; Spicyn, V. I. Scandium Chalcogenides. *Dokl. Akad. Nauk SSSR* **1961**, *141*, 364–367.
- (36) Assoud, A.; Kleinke, H. The Sesquiteralluride Sc₂Te₃. *Acta Crystallogr., Sect. E: Struct. Rep. Online* **2006**, *62*, i17–i18.
- (37) White, J. G.; Dismukes, J. P. The Crystal Structure of Scandium Sesquiteralluride. *Inorg. Chem.* **1965**, *4*, 1760–1763.
- (38) Caravati, S.; Bernasconi, M.; Parrinello, M. First-principles study of liquid and amorphous Sb₂Te₃. *Phys. Rev. B: Condens. Matter Mater. Phys.* **2010**, *81*, 014201.
- (39) Zhang, W.; Ronneberger, I.; Li, Y.; Mazzarello, R. Ab initio investigation of amorphous Sb₂Te. *Chem. Mon.* **2014**, *145*, 97–101.
- (40) Guo, Y. R.; Dong, F.; Qiao, C.; Wang, J. J.; Wang, S. Y.; Xu, M.; Zheng, Y. X.; Zhang, R. J.; Chen, L. Y.; Wang, C. Z.; Ho, K. M. Structural signature and transition dynamics of Sb₂Te₃ melt upon fast cooling. *Phys. Chem. Chem. Phys.* **2018**, *20*, 11768–11775.
- (41) Dronskowski, R.; Blochl, P. E. Crystal orbital Hamilton populations (COHP): energy-resolved visualization of chemical bonding in solids based on density-functional calculations. *J. Phys. Chem.* **1993**, *97*, 8617–8624.
- (42) Maintz, S.; Deringer, V. L.; Tchougréeff, A. L.; Dronskowski, R. Analytic projection from plane-wave and PAW wavefunctions and application to chemical-bonding analysis in solids. *J. Comput. Chem.* **2013**, *34*, 2557–2567.
- (43) Deringer, V. L.; Tchougréeff, A. L.; Dronskowski, R. Crystal orbital Hamilton population (COHP) analysis as projected from plane-wave basis sets. *J. Phys. Chem. A* **2011**, *115*, 5461–5466.
- (44) Sosso, G. C.; Caravati, S.; Bernasconi, M. Vibrational properties of crystalline Sb₂Te₃ from first principles. *J. Phys.: Condens. Matter* **2009**, *21*, 095410.
- (45) Löwdin, P. O. On the Non-Orthogonality Problem Connected with the Use of Atomic Wave Functions in the Theory of Molecules and Crystals. *J. Chem. Phys.* **1950**, *18*, 365–375.
- (46) Kresse, G.; Joubert, D. From ultrasoft pseudopotentials to the projector augmented-wave method. *Phys. Rev. B: Condens. Matter Mater. Phys.* **1999**, *59*, 1758.
- (47) Perdew, J. P.; Burke, K.; Ernzerhof, M. Generalized Gradient Approximation Made Simple. *Phys. Rev. Lett.* **1996**, *77*, 3865–3868.
- (48) Maintz, S.; Deringer, V. L.; Tchougréeff, A. L.; Dronskowski, R. LOBSTER: A tool to extract chemical bonding from plane-wave based DFT. *J. Comput. Chem.* **2016**, *37*, 1030–1035.
- (49) Kresse, G.; Hafner, J. Ab initio molecular dynamics for liquid metals. *Phys. Rev. B: Condens. Matter Mater. Phys.* **1993**, *47*, 558–561.
- (50) Wuttig, M.; Lüsebrink, D.; Wamwangi, D.; Welnic, W.; Gillessen, M.; Dronskowski, R. The role of vacancies and local distortions in the design of new phase-change materials. *Nat. Mater.* **2007**, *6*, 122–128.
- (51) Deringer, V. L.; Zhang, W.; Rausch, P.; Mazzarello, R.; Dronskowski, R.; Wuttig, M. A chemical link between Ge-Sb-Te and In-Sb-Te phase-change materials. *J. Mater. Chem. C* **2015**, *3*, 9519–9523.
- (52) Deringer, V. L.; Zhang, W.; Lumeij, M.; Maintz, S.; Wuttig, M.; Mazzarello, R.; Dronskowski, R. Bonding nature of local structural motifs in amorphous GeTe. *Angew. Chem., Int. Ed.* **2014**, *53*, 10817–10820.
- (53) Deringer, V. L.; Dronskowski, R.; Wuttig, M. Microscopic Complexity in Phase-Change Materials and its Role for Applications. *Adv. Funct. Mater.* **2015**, *25*, 6343–6359.
- (54) Konze, P. M.; Dronskowski, R.; Deringer, V. L. Exploring Chemical Bonding in Phase-Change Materials with Orbital-Based Indicators. *Phys. Status Solidi RRL* **2019**, *13*, 1800579.
- (55) Li, W.-L.; Ertural, C.; Bogdanovski, D.; Li, J.; Dronskowski, R. Chemical Bonding of Crystalline LnB₆ (Ln = La–Lu) and Its Relationship with Ln₂B₈ Gas-Phase Complexes. *Inorg. Chem.* **2018**, *57*, 12999–13008.
- (56) Kühne, T.; Krack, M.; Mohamed, F.; Parrinello, M. Efficient and Accurate Car-Parrinello-like Approach to Born-Oppenheimer Molecular Dynamics. *Phys. Rev. Lett.* **2007**, *98*, 066401.
- (57) Hutter, J.; Iannuzzi, M.; Schiffmann, F.; VandeVondele, J. cp2k: atomistic simulations of condensed matter systems. *Wiley Interdiscip. Rev.: Comput. Mol. Sci.* **2014**, *4*, 15–25.
- (58) Goedecker, S.; Teter, M.; Hutter, J. Separable dual-space Gaussian pseudopotentials. *Phys. Rev. B: Condens. Matter Mater. Phys.* **1996**, *54*, 1703.